

Research Article

Effect of Dispersoids and Intermetallics on Hardening the Al-Si-Cu-Mg Cast Alloys

J. Hernandez-Sandoval,¹ M. H. Abdelaziz ,² A. M. Samuel ,³ H. W. Doty,⁴
and F. H. Samuel ³

¹Facultad de Ingeniería Mecánica y Eléctrica, Universidad Autónoma de Nuevo Leon, San Nicolás de los Garza, Mexico

²Département PEC, Université Française d'Égypte, El Shorouk, Le Caire, Egypt

³Département des Sciences Appliquées, Université du Québec à Chicoutimi, Saguenay, Canada

⁴General Motors Materials Engineering, Warren, MI 48340, USA

Correspondence should be addressed to F. H. Samuel; fhsamuel@uqac.ca

Received 14 March 2021; Accepted 28 April 2021; Published 11 May 2021

Academic Editor: Jörg M. K. Wiezorek

Copyright © 2021 J. Hernandez-Sandoval et al. This is an open access article distributed under the Creative Commons Attribution License, which permits unrestricted use, distribution, and reproduction in any medium, provided the original work is properly cited.

The principal aim of the present research work was to compare the role of dispersoids Al_2O_3 (~15 μm average particle size) and SiC (~15 μm average particle size) with that offered by Zr- and Ni-based intermetallics (~35–70 μm average particle size) on the hardening of cast aluminum 354 alloy (9.1% Si, 0.12% Fe, 1.8% Cu, 0.008% Mn, 0.6% Mg, and 87.6% Al) at ambient temperature. There is no observable poisoning effect on the refinement of grain size after the addition of Zr to the alloys investigated in this study. The tensile test results were examined in light of the microstructural features of the corresponding alloy samples. The contribution of the added dispersoids or Ni and Zr alloying elements on the tensile properties of the 354 alloys was determined employing ΔP plots (where P = Property, UTS, YS, or %El), using the base alloy (in the as-cast condition) as a reference point. The tensile results were supported by investigating the precipitation-hardening phases using scanning and transmission electron microscopy as well as examining the fracture surfaces of selected conditions applying field emission scanning electron microscopy. The results show that, in all cases, Al_2Cu phase is the main hardening agent. The contribution of about 1.5 vol% of SiC or Al_2O_3 to the strength of the base alloy is higher than that offered by Zr- and Ni-based intermetallics, under the same aging treatment.

1. Introduction

Dispersoids are defined as small and numerous finely divided particles of one substance dispersed in another. Dispersoid particles are normally hard and brittle, resulting in excellent dispersion strengthening of the softer aluminum matrix [1]. According to Srinivasan and Imam [2], dispersoids are thermodynamically stable second-phase particles. Their size is in the range of 0.1 to 1.0 μm , which is made use of to reduce the alloy grain size. Fracture of these particles under loading can lead to the nucleation of cracks ahead of the main advancing crack. The effect of Cr and Mn addition and heat treatment on AlSi3Mg casting alloy was investigated by Tocci et al. [3] who found that Cr- and Mn-based dispersoid particles improve Vickers microhardness of the

aluminum matrix compared to the base alloy after solution treatment and quenching, which is in accordance with the dispersion-hardening mechanism. In a similar study, Remøe et al. [4] recommended decreasing heating rates which would increase the dispersoid density.

Dispersoids were also described as particles that form during ingot preheating caused by precipitation of the transition elements Cr, Mn, or Zr in the form of $\text{Al}_{12}\text{Mg}_2\text{Cr}$, $\text{Al}_{20}\text{Cu}_2\text{Mn}_3$, or $\text{Al}_{12}\text{Mn}_3\text{Si}$ and Al_3Zr particles, respectively [5]. A significant increase in mechanical properties of the tested hypoeutectic alloys was obtained by supersaturation of the Al phase with high melting point elements during HPDC processing of AlSi9Cu3(Fe) alloy as reported by Szymczak et al. [6]. A study of dispersoid particles in two Al-Mg-Si 6xxx-type aluminum alloys and their effects on

the recrystallization was conducted by Hichem and Rebai [7]. Their main conclusion was that the incorporation of Si in the metastable Al_3Zr type of dispersoid particles could increase the nucleation rate by reducing the volume-free energy of formation of the dispersoid particles. Kenyon et al. [8] added that changing the dispersoid volume fraction, size, and morphology has important implications for the pinning effectiveness of the dispersoids.

It is necessary to produce a microstructure containing thermally stable and coarsening-resistant dispersoids in order to enhance the mechanical properties of an aluminum alloy, in particular at high temperatures. The dispersoids or particles play an important role in resisting coarsening if the energy of their interface with the matrix, diffusivity, and solubility is low. The Al_3Zr particles are resistant to dissolution and coarsening; they can also control the evolution of the grain and subgrain structure, thereby making it possible to increase strength and ductility in the precipitation-hardened T6 condition [9–12]. The effectiveness of the dispersoids depends on their size, spacing, and distribution. In direct-chill cast alloys, the alloying elements are highly segregated following solidification [13–15].

According to Szajewski et al. [16], three different types of dislocation-precipitate interactions could occur depending on the nature of the precipitates, i.e., whether they are coherent or noncoherent. Strengthening by coherent precipitates is caused by distortion in the crystal lattice, representing barriers to dislocation movement [17–20]. Several research articles [6, 8, 21–23] emphasized that binary dispersoids such as Al_3Zr can be less effective due to limitations encountered during conventional manufacturing processes. Improvements can be achieved through the transformation of these binary trialuminides into ternary or quaternary forms by alloying with appropriate elements.

Previously, the present authors discussed the effect of addition of SiC and Al_2O_3 particulates on the microstructure and tensile properties (mainly quality index values as a function of thermal treatment) of Al–Si–Cu–Mg cast alloys [23]. In addition, the authors analyzed the effect of different alloying elements on the performance of this family of alloys over several publications [24–28]. The subject was readdressed in the present work to highlight the difference in the effectiveness of dispersoids, mainly Al_2O_3 , SiC and Al_3Zr , compared to intermetallics offered by the addition of Zr and Ni in the amounts of 0.25 wt.% and 0.5 wt.%.

2. Experimental Procedure

Alloy 354 modified with 200 ppm strontium and grain-refined using 0.25 wt% Ti (added using Al-5%Ti-1%B master alloy) was used as the base alloy (coded alloy A). The chemical composition in wt. % of the as-received 354 alloy ingots is listed in Table 1.

2.1. Additions.

- (i) The addition of Al_2O_3 particles was carried out using a metal matrix composite (6061 alloy + 20 vol % Al_2O_3) having a 2-to-30 μm particle size.

TABLE 1: Chemical composition of the as-received 354 alloy.

Element (wt %)					
Si	Fe	Cu	Mn	Mg	Al
9.1	0.12	1.8	0.0085	0.6	87.6

- (ii) The addition of SiC particles was done using a (359 alloy + 20 vol % SiC) metal matrix composite having a similar particle size.
- (iii) Zirconium and nickel additions were made using Al-20wt% Zr and Al-20wt% Ni master alloys, respectively.

Alloy A, with a chemical composition as shown in Table 1, was melted in an electrical furnace at 780°C, using a 60 kg SiC crucible. The molten alloy was degassed using pure, dry argon injected into the melt for 20 min by means of a graphite impeller rotating at 135 rpm. Grain refining and modification of the melt were carried out using Al-5% Ti-1% B and Al-10% Sr master alloys, respectively, to obtain levels of 0.25 wt.% Ti and 200 ppm Sr in the melt. Table 2 lists the chemical composition of the alloys which were investigated. The melt was poured into a preheated ASTM B-108 permanent mold (preheated to 460°C), to prepare test bars; the dimensions of which are shown in Figure 1. Three samples for chemical analysis were also taken at the time of the casting; this was done at the beginning, in the middle, and at the end of the casting process to ascertain the exact chemical composition of each alloy.

As will be mentioned in a later subsection, heat treatment of the test bars used for tensile testing involved solution heat treating them at 495°C for 8 hours, followed by quenching in warm water at 60°C, after which artificial aging was applied. In the present work, three aging temperatures (155°, 190°, and 350°C) and different aging times, up to 1000 h were used. After aging, the test bars were allowed to cool naturally at room temperature (25°C). All heat treatments were carried out in an air-forced Lindberg Blue M electric resistance furnace. All of the samples, whether as-cast, solution heat-treated, or aged, were tested to the point of fracture using an MTS servo-hydraulic mechanical testing machine at a strain rate of $4 \times 10^{-4} \text{ s}^{-1}$.

Ten samples from each condition were tested, for a total of 80 conditions for each alloy. Three other conditions were tested for each alloy corresponding to 200 h, 600 h, and 1000 h aging times, from which would be selected one specific aging temperature (190°C); this will be explained in detail further on in the text. The values for the mechanical properties, namely, ultimate tensile strength (UTS), yield strength (YS), and percent elongation (% El), were gathered from the computerized system of the MTS machine.

Samples for metallography were sectioned from the tensile-tested bars of all the alloys studied, about 10 mm below the fracture surface; they were then individually mounted in Bakelite and subsequently polished to a fine finish using 1 μm diamond suspension. The instrument used in this study was a Hitachi-SU-8000 FESEM, equipped with a standard secondary electron detector (SE), a backscatter electron detector (BSD), and an energy dispersive X-ray

TABLE 2: Chemical composition of the 354 alloys used in this study (wt.%).

Alloy/Element	Si	Fe	Cu	Mn	Mg	Ti	Sr (ppm)	Ni	Zr	Al ₂ O ₃ (volume%)	SiC (volume%)
A*	9.43	0.08	1.85	0.01	0.49	0.22	150	~	~	—	—
B	9.43	0.08	1.85	0.01	0.49	0.21	165	—	—	~1.5	—
C	9.43	0.08	1.85	0.01	0.49	0.19	170	—	—	—	~1.5
D	9.16	0.08	1.84	0.01	0.49	0.22	149	0.46	~	—	—
E	9.10	0.07	1.83	0.00	0.49	0.21	145	~	0.39	—	—
F	9.10	0.08	1.86	0.00	0.46	0.22	132	0.40	0.39	—	—
G	9.01	0.08	1.85	0.00	0.45	0.21	137	0.21	0.19	—	—

*354 base alloy; Ni, Zr, and dispersoid additions are highlighted in bold.

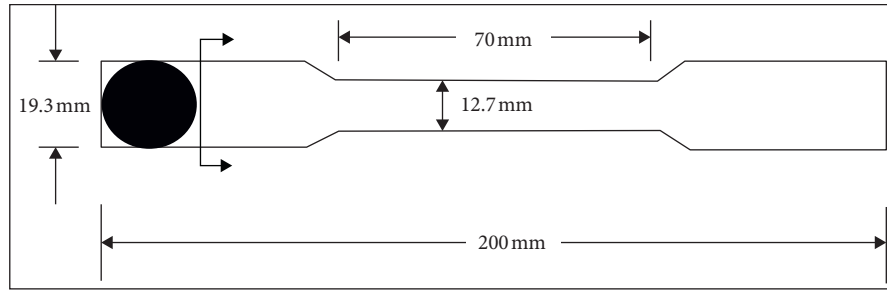


FIGURE 1: Dimensions of the tensile test bar.

spectrometer (EDS). The FESEM was operated at a voltage of 15 kV, with a maximum filament current of 3 amperes.

Transmission electron microscopy was used in order to observe and identify the strengthening precipitates in heat-treated samples and also to investigate the coherency of the precipitates with the matrix. The FEI Tecnai G² F20 electron microscope employed was equipped with an advanced control system which permits the integration of an EDAX[™] chemical analysis system, scanning transmission electron microscopy (STEM), and electron energy loss spectroscopy (EELS). The microscope was operated at an accelerating voltage of 200 kV.

3. Results and Discussion

In the present work, we are referring to the Al₂O₃ or SiC particulates as dispersoids in composites B and C containing these particulates since these particulates have no solubility in the matrix, maintaining at the same time uniform spacing. On the contrary, intermetallics are phases/compounds made up of two or more elements, producing a new phase with its own composition, crystal structure, and properties (Alloys D-G). Alloy A is the base alloy.

3.1. Microstructural Characterization. Figure 2(a) shows the microstructure of alloy A in the as-cast condition, revealing almost no presence of porosity. The blue arrows point to the change in the morphology of dendrites from elongated ones to a more rounded (rosetta-like) form which enhances feeding of the interdendritic regions, reducing the porosity in the grain-refined alloy as clearly displayed in Figure 2(b), a high-magnification micrograph of Figure 2(a). According to Campbell and Tiryakioğlu [29], based on the work of Fuoco

et al. [30], at an early stage of solidification, the dendrites can move as a slurry. Later, when eutectic freezing starts, the dendrites are fully solidified and fixed (about 45% remaining liquid) so that significant mobility of the eutectic is to be expected. However, after adding Sr, no mobility of the residual liquid is observed even at the high level of 45%. This explanation, in addition to the change in the dendrite shape presented in Figure 2(b), contradicts the model presented by Argo and Gruzleski [31] which suggests that, in unmodified alloys, the eutectic is characterized by its irregular solid/liquid interface, leading to entrapping of small pockets of liquid between advancing solidification fronts, causing the formation of microporosity. Figures 2(c) and 2(d), respectively, exhibit the distribution of the added Al₂O₃ and SiC particulates throughout the matrix, following solutionizing at 495°C for 8 h (SHT) revealing the complete dissolution of the Al₂Cu phase. Figures 3 and 4 reveal the adherence (no debonding) between the particulates and the surrounding matrix.

In alloy D, as the Al₃Zr precipitate must be present before the peritectic reaction, the formation of Al₃Zr from liquid is called a properitectic reaction [32, 33]. In the present work, the Zr concentration used was 0.2 wt.% and 0.4 wt.% for alloy G and alloys E-F, respectively. From Figure 5(a), the liquidus temperature should be 718°C and 780°C, respectively. The melt was maintained at 780°C, to avoid reaching the softening point of the SiC crucible. Thus, in the present case, Zr-rich phases will be precipitated in the form of intermetallics as well as dispersoids (alloys E and F), whereas in the case of alloy G, most of the Zr will be precipitated in the form of Al₃Zr dispersoids.

It should be borne in mind that the present alloys contain at least 15 elements and that the solidification rate was approximately 8°C/s. These two criteria make it difficult

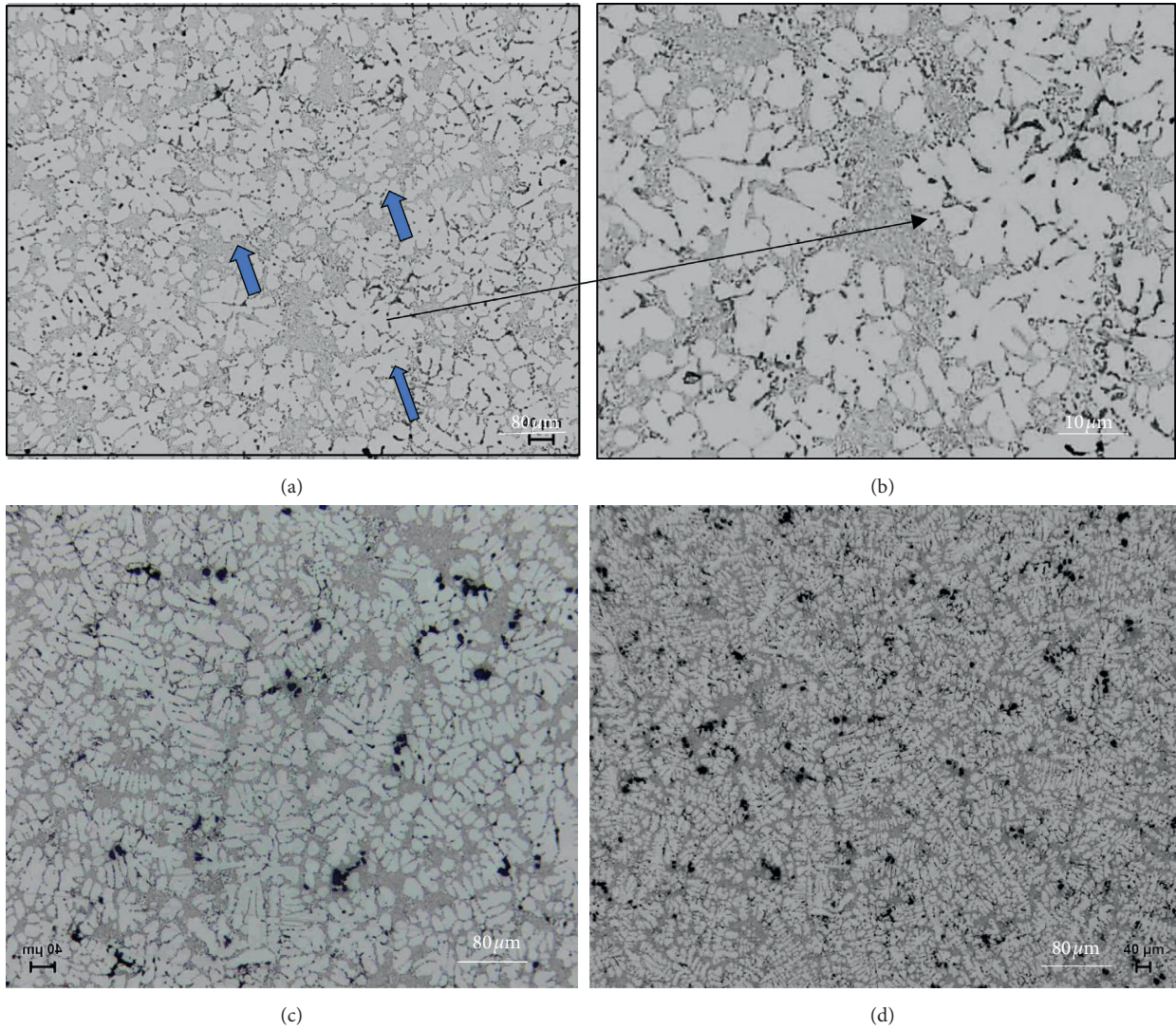


FIGURE 2: Optical microstructures of (a) alloy A, as cast, (b) a high-magnification micrograph of (a), (c) composite B-SHT, and (d) composite C-SHT.

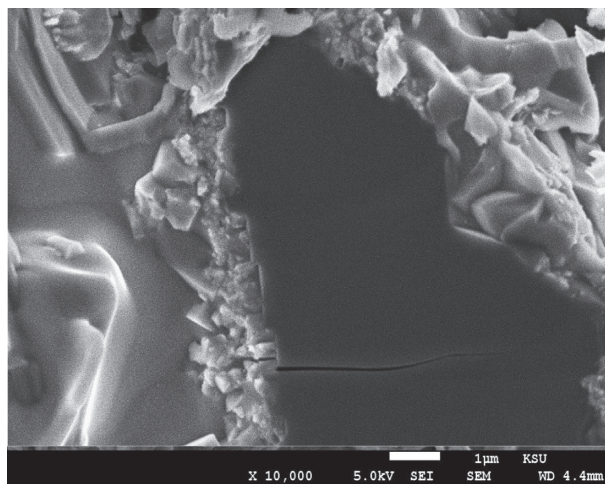


FIGURE 3: Secondary electron image of fracture surface of as-cast composite B.

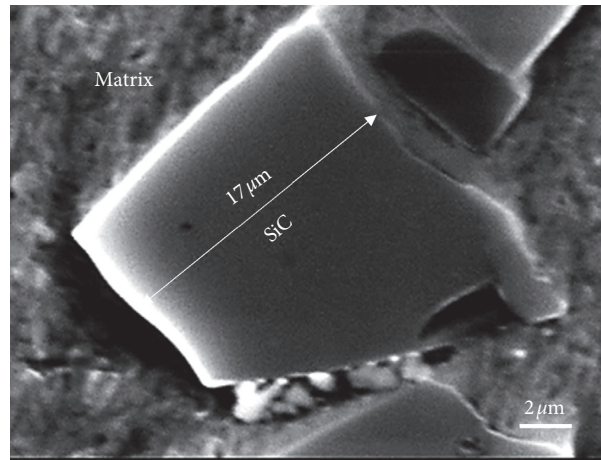
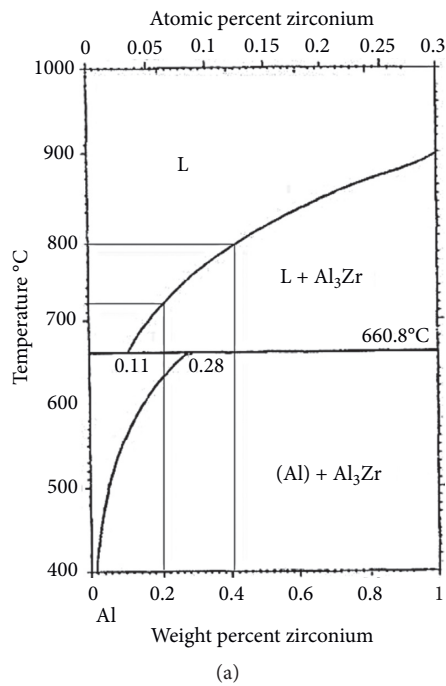
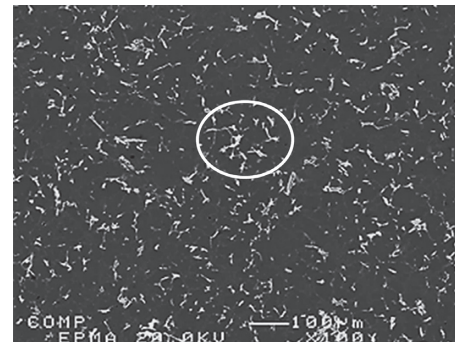


FIGURE 4: High-magnification secondary electron image of composite C. Note the absence of a gap between the SiC particle and the surrounding matrix.



(a)



(b)

FIGURE 5: (a) Al-rich corner of Al-Zr binary phase diagram [33] showing the percentages of Zr used in the present study and (b) backscattered electron micrograph of alloy D solidified at the rate of $\sim 0.35^\circ\text{C/s}$.

to strictly follow the binary equilibrium diagram shown in Figure 5(a). Figure 5(b) depicts the Zr-rich phase distribution in alloy D in the as-cast condition, solidified at a very slow rate $\sim 0.35^\circ\text{C/s}$. In this case, the chemical composition of the dispersoid is Al-Zr-Ti as inferred from the associated EDS spectrum displayed in Figure 6(a). In the presence of Ti in the matrix, Zr has a strong affinity to react with Ti forming $\text{Al}_3(\text{Zr}, \text{Ti})_5$ [34–36] or $\text{Al}_3(\text{Zr}_{1-x}\text{Ti}_x)$ dispersoids [36]. Figure 7 depicts the precipitation of Al_3Zr dispersoids in alloy D in the as-cast condition, in a sample prepared from a tensile test bar solidified at about 8°C/s . According to Ikhtlaq et al. [34], Zr has a preferred orientation (002) along other

significant diffraction planes (100), (101), (102), and (110) of Zr confirming the hexagonal crystal structure as shown in Figure 6(b).

Figure 8 displays the progress in the size and distribution of the Al_2Cu precipitation hardening particles (main hardening agent) at 190°C (peak aging). It is evident from Figures 8(b) and 8(c) that with increase in the aging time, there is an increase in the size of the precipitated Al_2Cu particles coupled with change in their morphology from spherical to short rods, which leads to a gradual decrease in contribution of these precipitates to both UTS and YS regardless the alloy type, reaching almost nil after 1000 h [37].

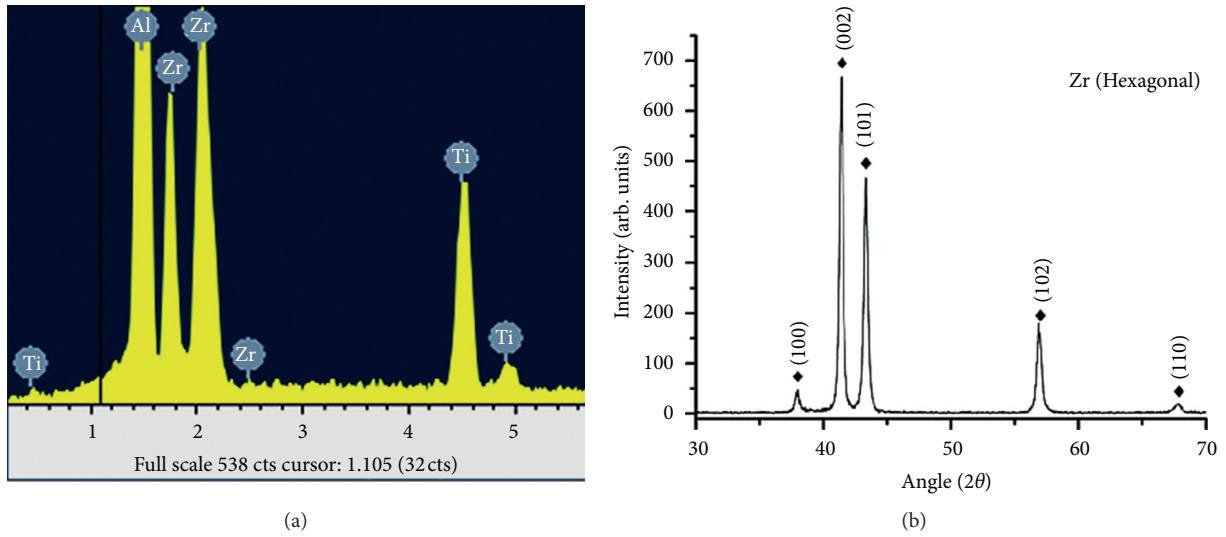
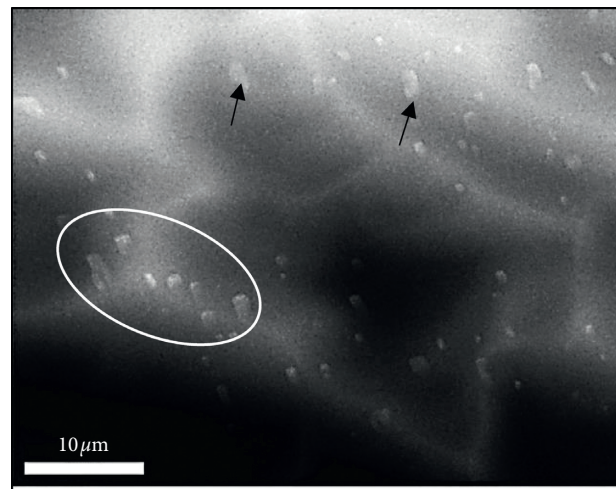
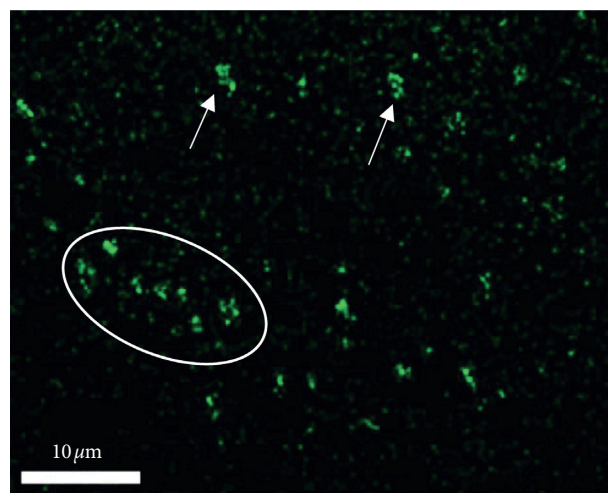


FIGURE 6: (a) EDS spectrum corresponding to white circled area in Figure 5(b) showing strong reflections from Al, Zr, and Ti and (b) X-Ray diffraction spectrum for zirconium metal [34].

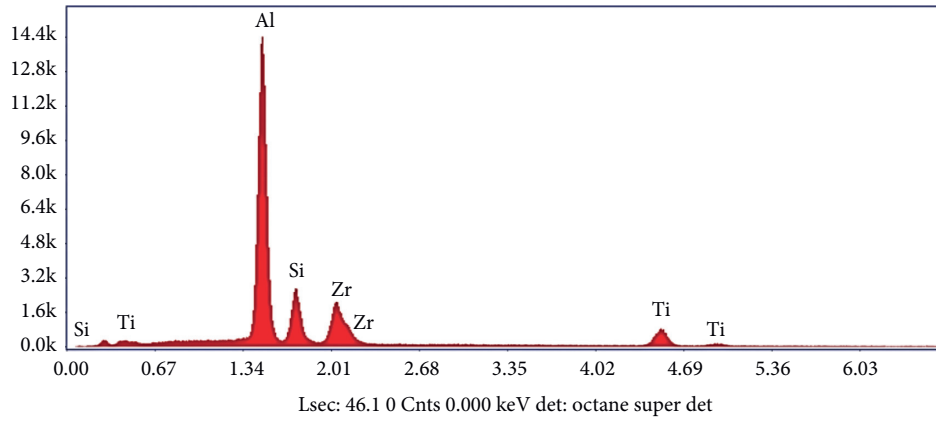


(a)



(b)

FIGURE 7: Continued.

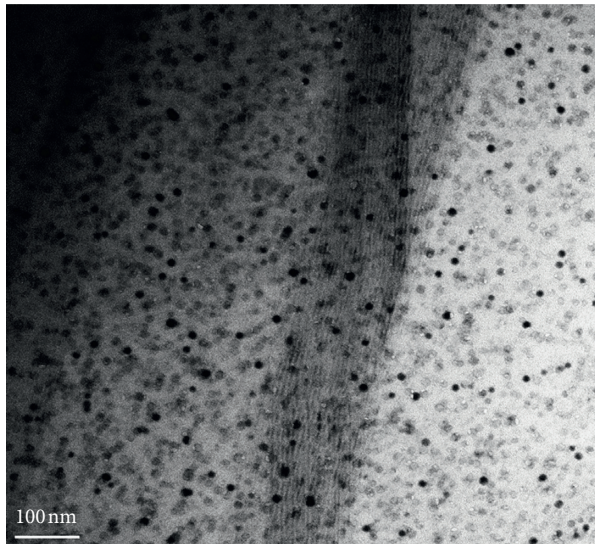


(c)

Element	Weight %	Atomic %	Net Int.	Error %	Kratio	Z	R	A	F
AlK	48.15	63.08	2,523.32	3.35	0.48	1.09	0.96	0.9	1.01
SiK	11.16	14.05	457.67	5.50	0.10	1.11	0.97	0.76	1.01
ZrL	20.42	7.91	344.71	5.08	0.15	0.81	1.13	0.88	1.01
TiK	20.27	14.95	199.60	5.56	0.19	0.93	1.01	0.98	1.02

(d)

FIGURE 7: (a) Bright field electron micrograph of the precipitation of Al-Zr-Ti dispersoids in alloy D in the as-cast condition, (b) map of Zr distribution in (a), (c) EDS spectrum corresponding to white circle in (a), and (d) approximate composition of particles in (a). The average size of Zr-rich precipitates in (a) is about 20–30 nm.



(a)



(b)

FIGURE 8: Continued.

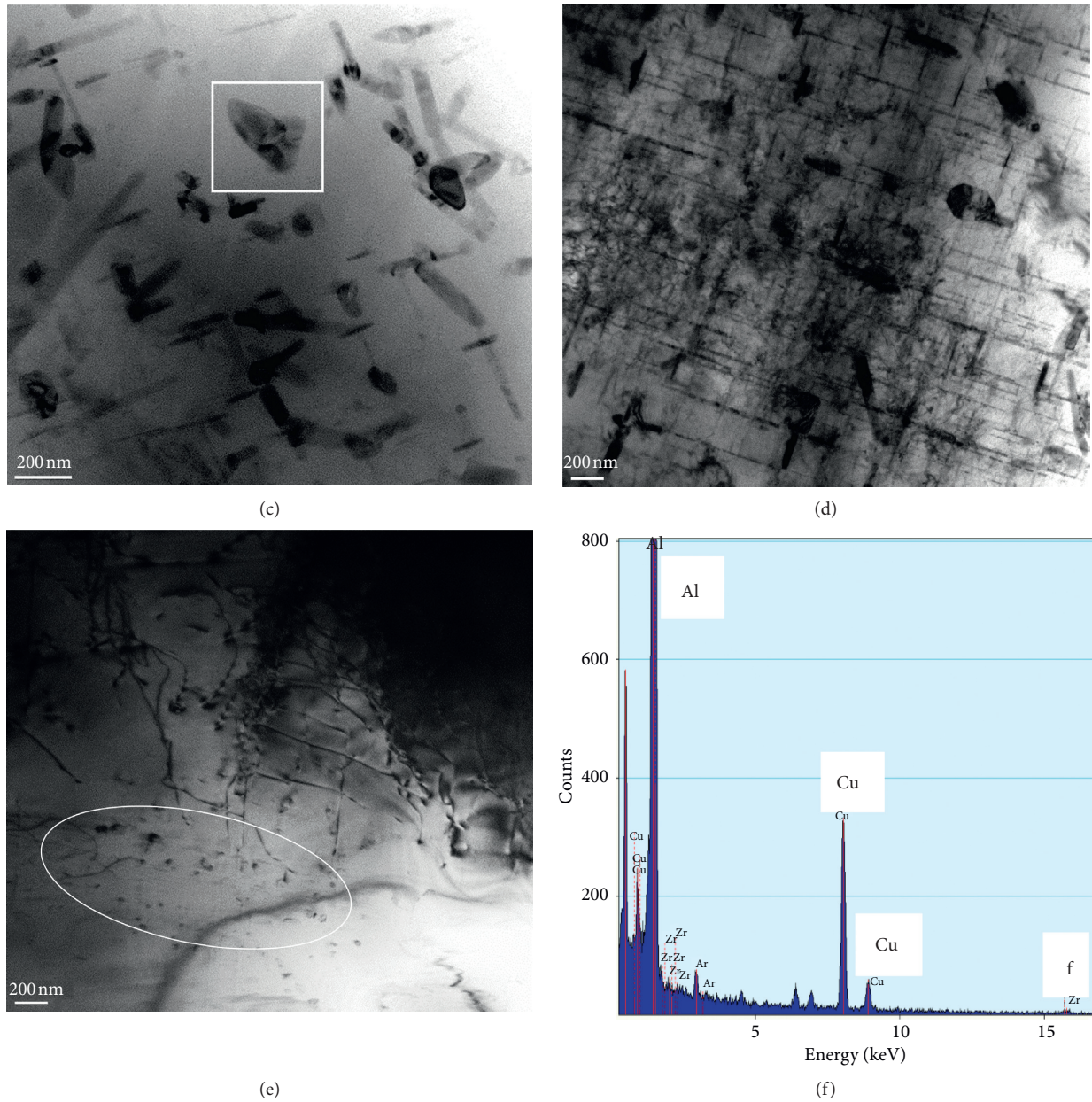


FIGURE 8: Bright field electron micrographs showing the progress in the size and distribution of the precipitated second phase during aging at 190°C. (a) 2 h, (b) 200 h, (c) 1000 h, (d) dislocation/particle interactions in condition (c), note the high dislocation density, (e) dislocation density in alloy A after solutionizing treatment, note the size of the precipitated particles in the white area, and (f) EDS spectrum corresponding to square area in (c) revealing Al and Cu peaks.

Figure 8(d) shows dislocation/precipitate interactions; note the significant increase in the dislocation density compared to that after solutionizing treatment (Figure 8(e)). Figure 8(f) presents the EDS spectrum, corresponding to the white square area in Figure 8(c), indicating reflections due to Al and Cu.

3.2. Tensile Properties. Table 3 lists the tensile parameters of alloy A in the as-cast condition. Figure 9 presents the contribution of added particulates or alloying elements on the tensile properties of the 354 alloys B through G, using

TABLE 3: Tensile properties of alloy A in the as-cast condition.

Parameter-	UTS (MPa)	YS (MPa)	%El
Value	235	154	1.6

alloy A in the as-cast condition as a reference point. It should be mentioned here that, in a previous study, the authors reported on the aging behavior of alloy A in the temperature range 155°C–350°C for times up to 100 h [38].

As can be seen in Figure 9(a), when the alloys were aged at 155°C for 2 h, composite B (containing maximum 1.5 vol%

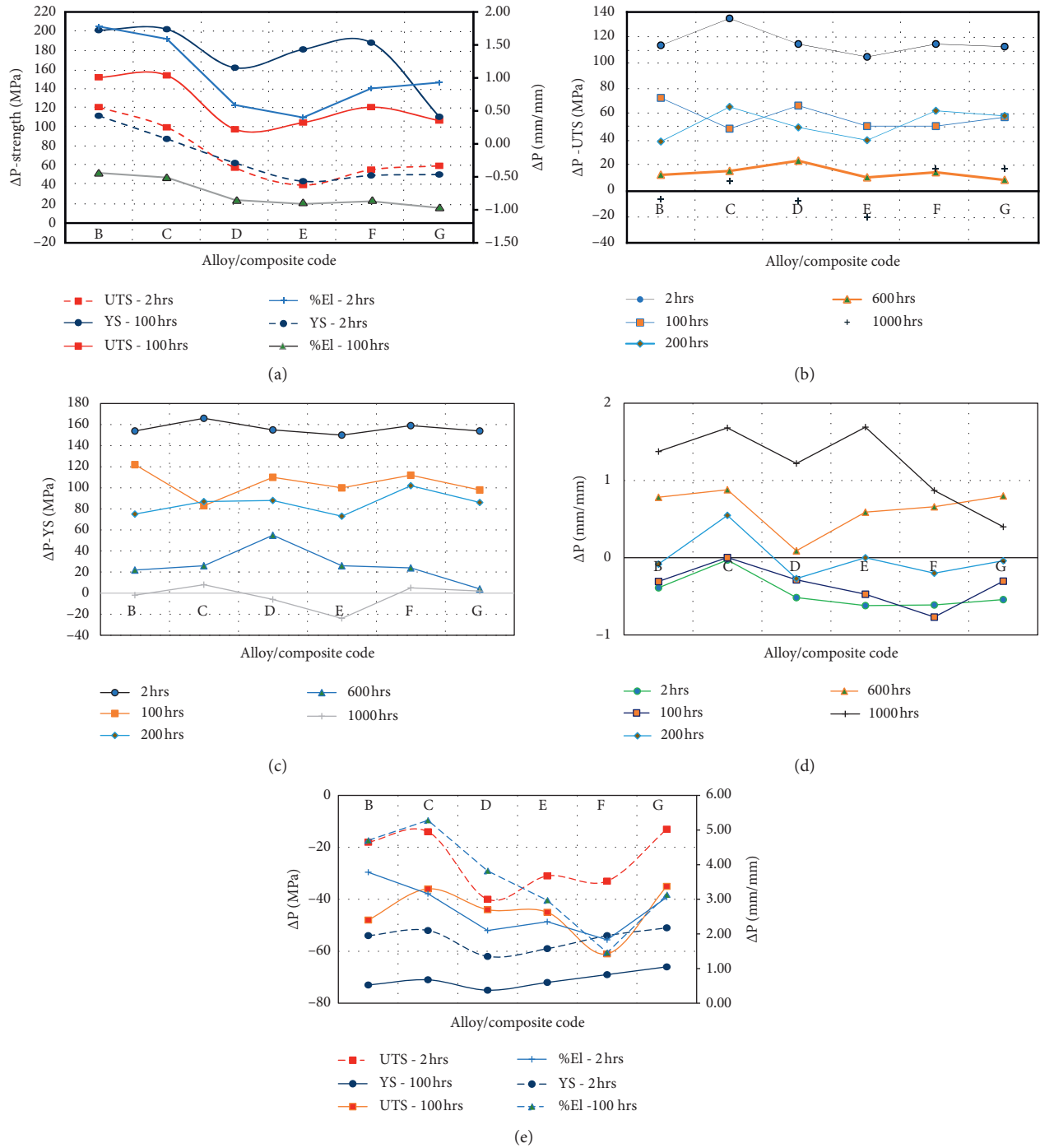


FIGURE 9: Variation in ΔP as a function of aging condition: (a) 155°C, (b) UTS-190°C, (c) YS-190°C, (d) % El-190°C, and (e) 350°C.

Al_2O_3) contributed significantly to the UTS of alloy A (about 120 MPa) followed by a linear decrease up to alloy E (40 MPa) beyond which other alloys (alloys F and G) showed a slight increase in UTS, going to 56 and 60 MPa, respectively. Aluminum oxide particulates are a ceramic compound with a hexagonal crystal lattice. The oxygen anions define a hexagonal close packed structure, and the aluminum cations occupy 2/3 of the octahedral sites in the hcp lattice. It is used for its hardness and strength, about 9 on the Mohs scale of mineral hardness (just below diamond) [34].

Although SiC (composed of tetrahedra of carbon and silicon atoms with strong bonds in the crystal lattice) is a very hard and strong material [39], its contribution is slightly lesser than that of Al_2O_3 which may be interpreted in terms of the actual particulate volume fraction. However, both composites B and C offered a better resistance to softening, yield strength, as well as a better improvement in the alloy ductility compared to those obtained from the other alloys containing Ni or Zr. Figures 9(b) to 9(d) demonstrate the variation in the UTS, YS, and % elongation, respectively,

when both particulates and alloying elements were added to alloy A. The tensile bars were exposed to aging at 190°C for times up to 1000 h.

A comparison of Figures 9(b) and 9(c) shows that the contribution level to the alloy YS is higher than that to the UTS. Although the contribution to the ductility of alloy A in Figure 9(d) followed a similar pattern as those for UTS and YS, a sharp decrease in the %El was observed for alloys F and G (1000 h). On the contrary, low aging times (2 h–100 h) resulted in a negative change in the % elongation. Some improvement can be seen for alloy G that contains 0.25% Zr + 0.25% Ni producing same levels as composites B and C due to precipitation of Al_3Zr dispersoids.

Daoud and Reif [40] suggested that the hardening process is significantly affected by the presence of micro-oxides, carbides, or SiC. The precipitation takes place on the dislocation lines. As a result of the mismatch between the coefficient of thermal expansion of the matrix and the reinforcement, it is not expected to alter the precipitation sequence. Samuel et al. [41] proposed that the relative amount of hardening precipitates is also influenced by the added dispersoids. In order to achieve a significant improvement in the alloy strength, the authors recommended increasing the reinforcement particulates by an order of magnitude than those used in composites B and C. Apparently, the added amounts of Al_2O_3 or SiC in the present study have a marginal effect on the composite tensile properties compared to Zr and Ni addition.

As will be observed from Figure 10, the highest standard deviations with respect to UTS are exhibited by the alloys containing micro-oxides; also, the variations are more accentuated for the temperatures where the maximum strength values were observed, i.e., at 155°C and 190°C. This figure is showing the average standard deviation values for all alloys studied, where the higher standard deviation values may be observed for the properties pertaining to composites B and C. In Figure 11, the maximum standard deviations correspond to the maximum ductility values, observed at 155°C and 350°C for alloys containing micro-oxides/carbides. In both Figures 10 and 11, the tensile test values corresponding to these two temperatures reveal the highest standard deviations, particularly for composites B and C, when the seven alloys used in this study are subjected to comparison.

3.3. Fracture Behavior. Figure 12(a) represents the fracture surface of alloy A in the as-cast condition (secondary electron image) where severe cracks (arrowed blue) can be seen propagating through the fine-dimpled structure (1.3% elongation). Solutionizing at 495°C for 8 h resulted in a significant increase in the alloy ductility (6.3%) which reflected on the alloy surface fracture as displayed in Figure 12(b) where a deep dimple structure is seen predominating the fracture surface—blue arrows. Slip bands are observed covering the wall of the dimples shown in Figure 12(b). Figure 12(c) exhibits the fracture surface of alloy A aged at 190°C for 2 h revealing severe cracks (white arrows), whereas similar features as those shown in

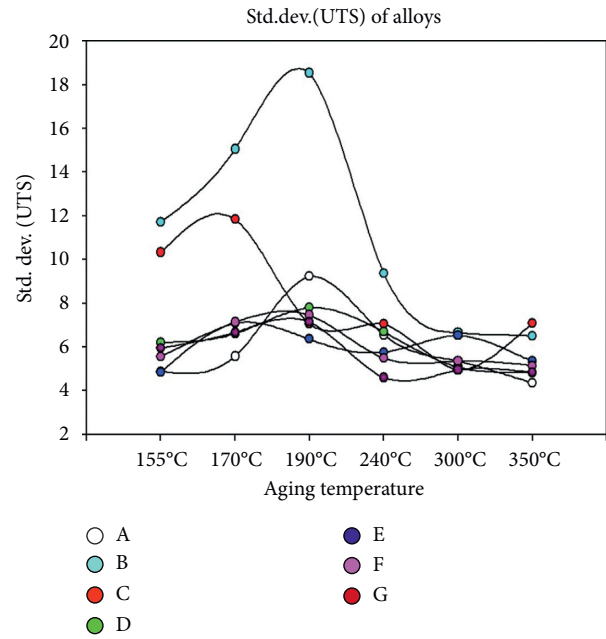


FIGURE 10: Mean standard deviation of the UTS values observed for the five alloys and two composites studied.

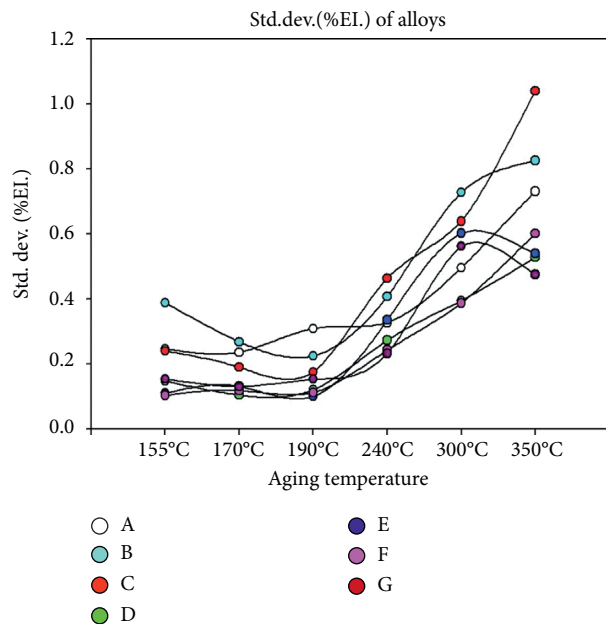


FIGURE 11: Mean standard deviation of the % elongation values observed for the five alloys and two composites studied.

Figure 12(b) were reported covering the fracture surface when the alloy was aged at 350°C for 100 h (overaging), see arrows in Figure 12(d). In composite C, Figure 13, the presence of micro-SiC particulates were seen at the bottom of the coarse dimples (white arrows) when the alloy was solutionized (reaching 5.3% ductility). In all solutionized alloys, clear slip bands were commonly observed as shown by the blue arrows in the figure. The fracture surface of alloy D (containing 0.4%Zr) after solutionizing treatment resulted

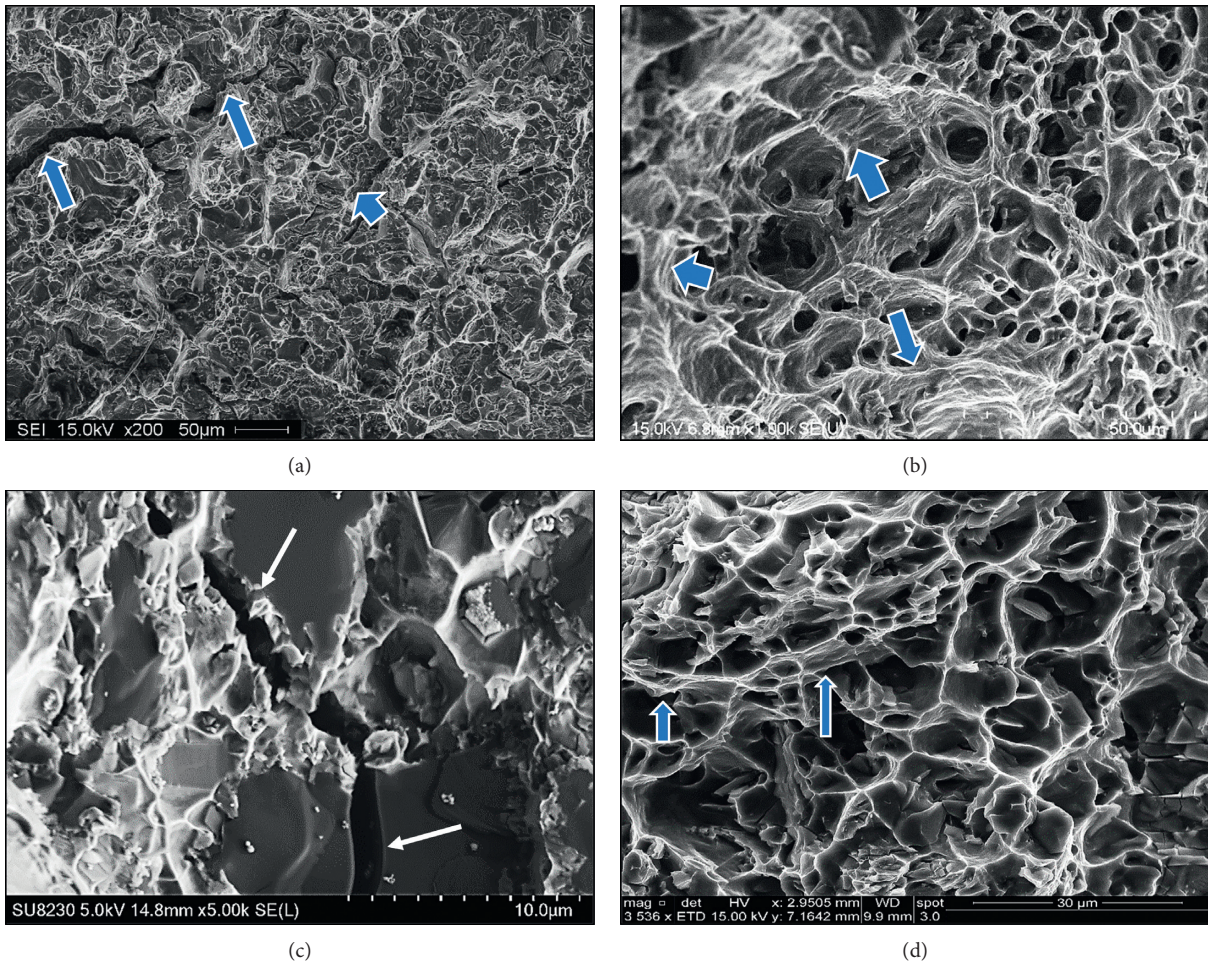


FIGURE 12: Secondary electron images (SEI) of the fracture surface of alloy (A). (a) as-cast condition (1.3% El), (b) SHT condition (6.2% El), (c) alloy A aged 2 h at 190°C (1.7%El), and (d) alloy A aged 100 h at 350°C (5.8%El).

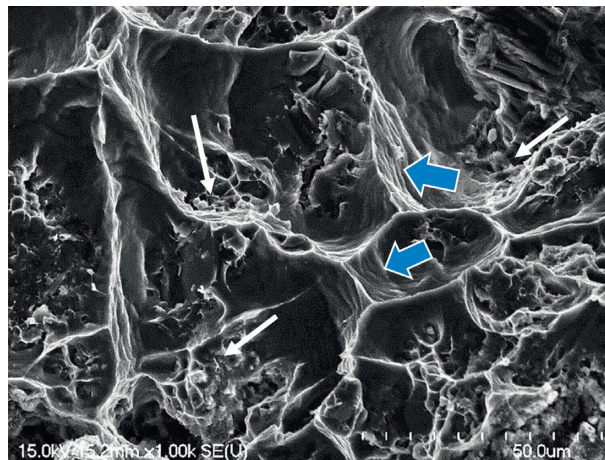


FIGURE 13: SEI of the fracture surface of composite C in the SHT condition (5.3%El).

in enhancing the alloy ductility, reaching about 4.5%. While the SHT did not change the shape of the star-like particles, Figure 14(a) shows several slip lines clearly visible on the edges (black arrows) of the particle, as well as a long crack reaching the star center (white dashed arrow). The associated

EDS spectrum, Figure 14(b), exhibits reflections due to Al, Si, Zr, and Ti elements suggesting that the composition of this phase is $(Al, Si)_2(Ti, Zr)$ [28].

Figure 15(a) demonstrates the fracture of alloy E in the as-cast condition. It is evident that the presence of such a

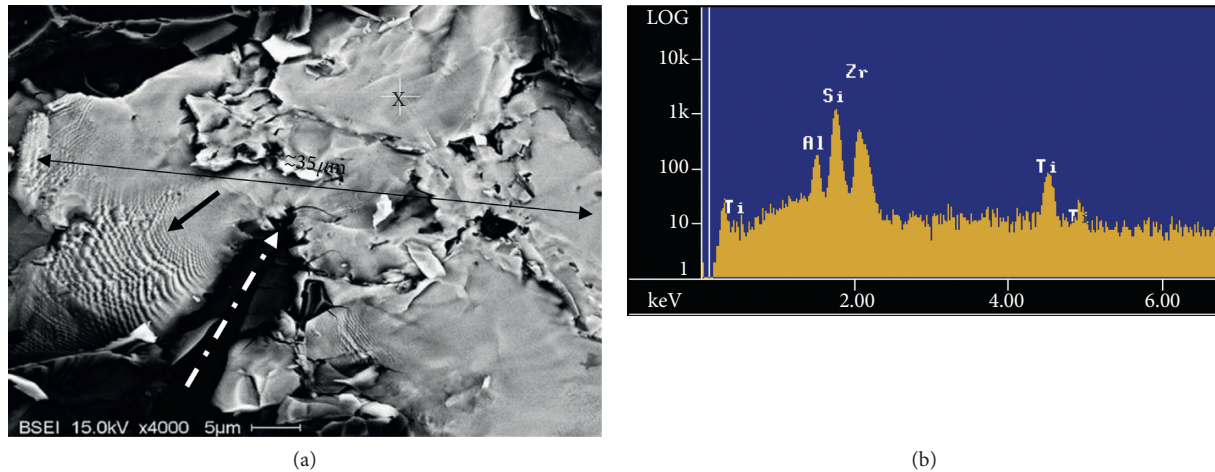


FIGURE 14: (a) Backscattered electron micrograph of alloy D after solutionizing treatment (4.5%El) and (b) EDS spectrum corresponding to the area marked X in (a), $(Al, Si)_2(Zr, Ti)$ phase.

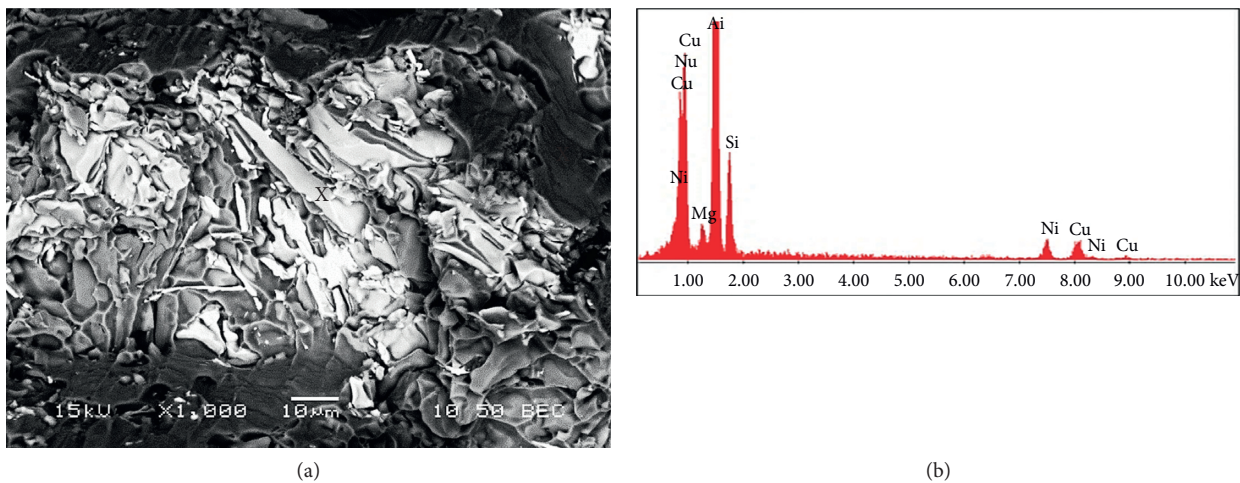


FIGURE 15: (a) SEI of fractured Ni-rich phase-alloy E (1.44%El) in the as-cast condition, note the platelet shape of the Ni-rich compounds and (b) EDS spectrum corresponding to (a).

significant amount of insoluble Ni-rich phases would cause marked brittleness (1.44%El). The associated EDS spectrum in Figure 15(b), corresponding to the marked spot in (a), shows strong peaks of Al, Ni, Cu, and Si with a small peak of Mg indicating a mixture of Al_3CuNi and $Q-Al_5Cu_2Mg_8Si_6$ phases. The fracture surface of alloy F (containing about 0.4%Ni + 0.45Zr) is illustrated in Figure 16(a) showing a fractured massive Zr-rich phase particle. The black arrow points to parallel markings on the surface of the particle. The associated EDS spectrum corresponding to the area marked X in (a) reveals that this phase is possibly $(Al, Si)_3(Ti, Zr)$, depending on the Si/Zr intensity ratio [42].

Based on the EDS spectra presented in Figures 7(c), 14(b), and 16(b), the Si/Zr intensity ratios are 0, 0.5, and 1, respectively, depending on the Zr-rich phase particle size. According to Garza-Elizondo et al. [43], the $(Al, Si)_2(Ti, Zr)$ phase contains 36 wt.% Si and 38 wt.% Zr, whereas the $(Al, Si)_3(Ti, Zr)$ phase contains 11 wt.% Si and 47 wt.% Zr,

reaching Al_3Zr when Si is practically nil. The atomic radii of Al, Si, Ti, and Zr are listed in Table 4. The Al_3Zr phase is a closed packed structure (Figure 17(a)) with an interatomic spacing of 0.441 nm. However, there is controversy regarding the particle structure which has been reported as being cubic $L1_2$ or tetragonal DO23, as shown in Figure 17(b) [42, 43]. It is also reported that Al_3Zr has the stable DO23 structure, but for small supersaturations of the solid solution, Al_3Zr precipitates with the metastable $L1_2$ structure and precipitates with the DO23 structure only appear for prolonged heat treatment and high enough supersaturations [44, 45].

It is suggested that since the Si atom has a small radius (Table 4) compared to the interatomic spacing in Figure 17(a), the Si atoms can easily diffuse into the Al_3Zr cells during the solidification process. The concentration of Si in the Al_3Zr phase particle is a function of the temperature and the size of the formed Al_3Zr phase particle. In other

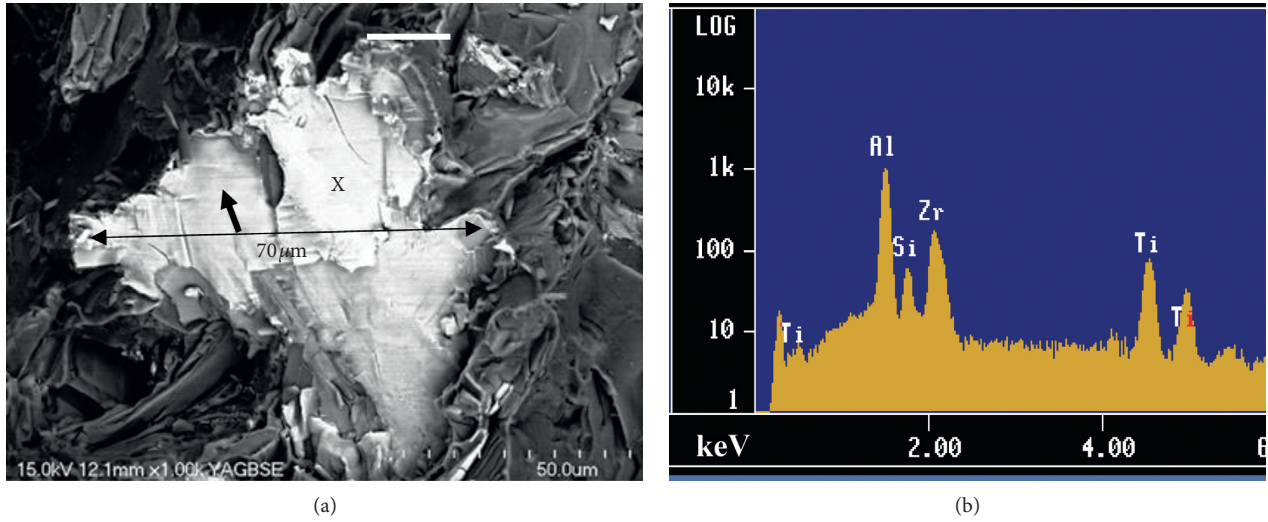


FIGURE 16: (a) Backscattered electron image of alloy F in the as-cast condition showing fracture of a massive Zr-rich phase, (b) EDS spectrum corresponding to the area marked X in (a), indicating $(Al, Si)_3(Zr, Ti)$ phase.

TABLE 4: Atomic radii of the main elements in $(Al, Si)(Zr, Ti)$ phases.

Element	Radius (nm)
Al	0.143
Si	0.117
Ti	0.145
Zr	0.160

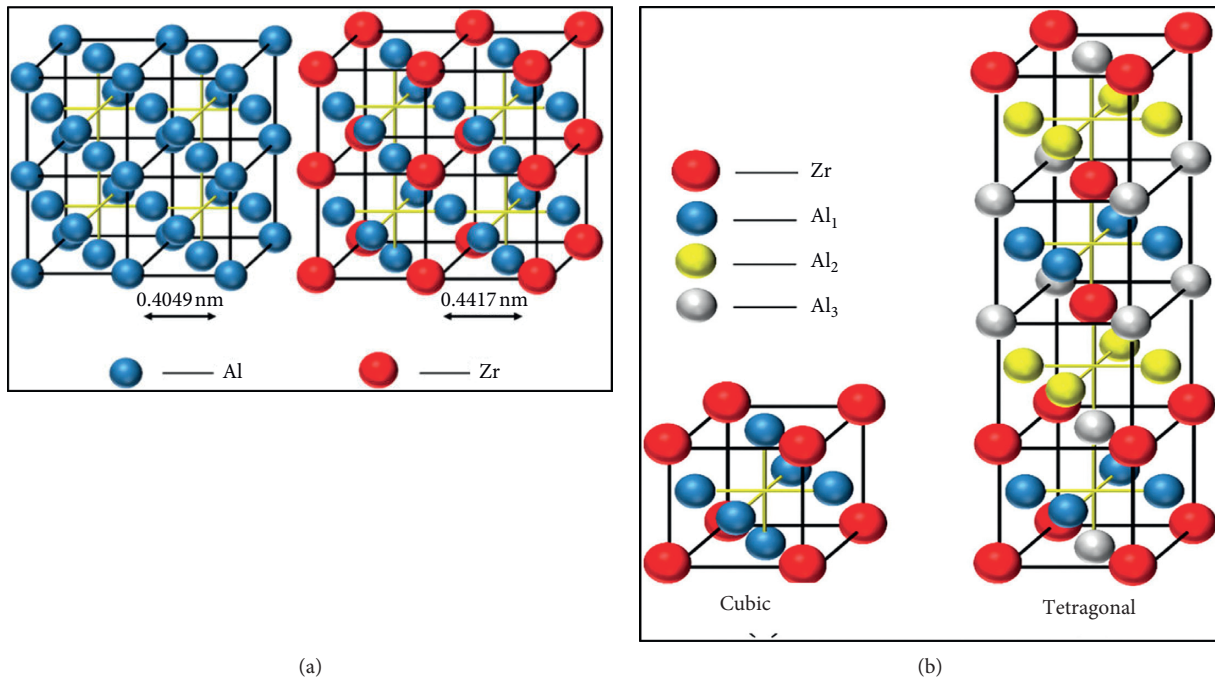


FIGURE 17: Suggested crystal structures of Al_3Zr [44, 45].

words, the larger the size of the Al_3Zr phase particle, the lesser is the Si concentration, as shown in Figure 16(b). Considering the atomic radius of Ti (0.145 nm) is very close to that of the Al atom (0.143 nm), this would facilitate the substitution of a certain number of Al atoms by Ti atoms.

4. Conclusions

Based on the results obtained in this study, the following conclusions may be drawn:

- (1) There is no observable poisoning effect on the refinement of grain size after the addition of Zr to the alloys investigated in this study.
- (2) The Si/Zr ratio varies depending on the size of Zr-rich phase particles.
- (3) The standard deviation (SD) of the UTS and %El values is higher in SiC and Al_2O_3 particulate-containing alloys due to their low volume fraction and tendency for segregation.
- (4) In order to achieve a lower SD, the volume fraction of Al_2O_3 or SiC particulates should be increased by an order of magnitude.
- (5) The results show that, in all cases, Al_2Cu phase is the main hardening agent. The contribution of about 1.5 vol.% of SiC or Al_2O_3 particulates to the strength of the base alloy is higher than that those offered by Zr- and Ni-based intermetallics.
- (6) The reduction in mechanical properties due to addition of different elements is attributed principally to the increase in the percentage of intermetallic phases formed during solidification; such phase particles would act as stress concentrators, decreasing the alloy ductility.

Data Availability

Data will be available upon request.

Conflicts of Interest

There are no conflicts of interest between the authors.

References

- [1] Y. Li and L. Arnberg, "Precipitation of dispersoids in DC-cast AA3103 alloy during heat treatment," in *Essential Readings in Light Metals*, J. F. Grandfield and D. G. Eskin, Eds., pp. 1021–1027, Springer, Cham, Switzerland, 2016.
- [2] R. Srinivasan and M. A. Imam, "Role of dispersoids on the fatigue behavior of aluminum alloys: a review," in *Fatigue of Materials III*, T. S. Srinivasan, M. A. Imam, and R. Srinivasan, Eds., pp. 11–22, Springer, Cham, Switzerland, 2016.
- [3] M. Tocci, R. Donnini, G. Angella, and A. Pola, "Effect of Cr and Mn addition and heat treatment on AlSi3Mg casting alloy," *Materials Characterization*, vol. 123, pp. 75–82, 2017.
- [4] M. Remøe, I. Westermann, and K. Marthinsen, "Characterization of the density and spatial distribution of dispersoids in Al-Mg-Si alloys," *Metals*, vol. 9, no. 1, p. 26, 2019.
- [5] N. C. W. Kuijpers, F. J. Vermolen, C. Vuik, P. T. G. Koenis, K. E. Nilsen, and S. v. d. Zwaag, "The dependence of the β -AlFeSi to α -Al(FeMn)Si transformation kinetics in Al-Mg-Si alloys on the alloying elements," *Materials Science and Engineering: A*, vol. 394, no. 1–2, pp. 9–19, 2005.
- [6] T. Szymczak, G. Gumienny, L. Klimek, M. Goły, J. Szymshal, and T. Pacyniak, "Characteristics of Al-Si alloys with high melting point elements for high pressure die casting," *Materials*, vol. 13, no. 21, p. 4861, 2020.
- [7] F. Hichem and G. Rebai, "Study of dispersoid particles in two Al-Mg-Si aluminium alloys and their effects on the recrystallization," *Applied Physics A*, vol. 119, no. 1, pp. 285–289, 2015.
- [8] M. Kenyon, J. Robson, J. Fellowes, and Z. Liang, "Effect of dispersoids on the microstructure evolution in Al-Mg-Si alloys," *Advanced Engineering Materials*, vol. 21, pp. 1–7, 2019.
- [9] T. Szymczak, J. Szymshal, and G. Gumienny, "Statistical methods used in the assessment of the influence of the Al-Si alloy's chemical composition on its properties," *Archives of Foundry Engineering*, vol. 18, pp. 203–211, 2018.
- [10] T. Szymczak, J. Szymshal, and G. Gumienny, "Evaluation of the effect of the Cr, Mo, V and W content in an Al-Si alloy used for pressure casting on its proof stress," *Archives of Foundry Engineering*, vol. 18, pp. 105–111, 2018.
- [11] T. Szymczak, J. Szymshal, and G. Gumienny, "Evaluation of the effect of Cr, Mo, V and W on the selected properties of silumins," *Archives of Foundry Engineering*, vol. 18, pp. 77–82, 2018.
- [12] M. Cai, J. D. Robson, and G. W. Lorimer, "Simulation and control of dispersoids and dispersoid-free zones during homogenizing an AlMgSi alloy," *Scripta Materialia*, vol. 57, no. 7, pp. 603–606, 2007.
- [13] K. Marthinsen, E. Nes, O. Daaland, and T. Furu, "The spatial distribution of nucleation sites and its effect on recrystallization kinetics in commercial aluminum alloys," *Metallurgical and Materials Transactions A*, vol. 34, no. 12, pp. 2705–2715, 2003.
- [14] C. D. Marioara, S. J. Andersen, T. N. Stene et al., "The effect of Cu on precipitation in Al-Mg-Si alloys," *Philosophical Magazine*, vol. 87, no. 23, pp. 3385–3413, 2007.
- [15] T. Marlaud, A. Deschamps, F. Bley, W. Lefebvre, and B. Baroux, "Influence of alloy composition and heat treatment on precipitate composition in Al-Zn-Mg-Cu alloys," *Acta Materialia*, vol. 58, no. 1, pp. 248–260, 2010.
- [16] B. A. Szajewski, J. C. Crone, and J. Knap, "Analytic model for the Orowan dislocation-precipitate bypass mechanism," *Materialia*, vol. 11, p. 10067, 2020.
- [17] S. Drouzy, Jacob, and M. Richard, "Interpretation of tensile results by means of quality index and probable yield strength," *AFS International Cast Metals Journal*, vol. 5, pp. 43–50, 1980.
- [18] C. H. Cáceres, *Microstructure Design and Heat Treatment Selection for Casting Alloys Using the Quality Index*, ASM-IMS, Cincinnati, OH, USA, 1999.
- [19] C. H. Cáceres, T. Din, A. K. M. B. Rashid, and J. Campbell, "Effect of aging on quality index of an Al-Cu casting alloy," *Materials Science and Technology*, vol. 15, no. 6, pp. 711–716, 1999.
- [20] C. H. Cáceres and J. A. Taylor, "Enhanced ductility in Al-Si-Cu-Mg casting alloys with high Si content," in *Shape Casting: The John Campbell Symposium*, M. Tiryakioglu and P. Crepeau, Eds., pp. 245–254, Los Angeles, CA, USA, 2005.
- [21] I. El-Mahallawi, A. Shash, and A. Amer, "Nanoreinforced cast Al-Si alloys with Al_2O_3 , TiO_2 and ZrO_2 nanoparticles," *Metals*, vol. 5, no. 2, pp. 802–821, 2015.

- [22] T. Dorin¹, M. Ramajayam, and T. J. Langan, "Effects of Mg, Si, And Cu on the formation of the Al₃Sc/Al₃Zr dispersoids," in *Proceedings of the 16th International Aluminum Alloys Conference (ICAA16)*, Canadian Institute of Mining, Metallurgy & Petroleum, Montreal, Canada, ISBN: 978-1-926872-41-4, Montreal, Canada, June 2018.
- [23] J. Hernandez-Sandoval, F. H. Samuel, and S. Valtierra, "Effect of additions of SiC and Al₂O₃ particulates on the microstructure and tensile properties of Al-Si-Cu-Mg cast alloys," *International Journal of Metalcasting*, vol. 10, no. 3, pp. 253–263, 2016.
- [24] G. H. Garza-Elizondo, A. M. Samuel, S. Valtierra, and F. H. Samuel, "Effect of transition metals on the tensile properties of 354 alloy: role of precipitation hardening," *International Journal of Metalcasting*, vol. 11, no. 3, pp. 413–427, 2017.
- [25] G. H. Garza-Eiizondo, S. A. Alkahtani, A. M. Samuel, and F. H. Samuel, "Role of Ni and Zr in preserving the strength of 354 aluminum alloy at high temperature," in *Light Metals 2014*, pp. 305–314, Minerals, Metals and Materials Society, San Diego, CA, USA, 2014.
- [26] H. R. Ammar, A. M. Samuel, F. H. Samuel, E. Simielli, G. K. Sigworth, and J. C. Lin, "Influence of aging parameters on the tensile properties and quality index of Al-9 pct Si-1.8 pct Cu-0.5 pct Mg 354-type casting alloys," *Metallurgical and Materials Transactions A*, vol. 43, no. 1, pp. 61–73, 2012.
- [27] A. M. Samuel, F. H. Samuel, and H. W. Doty, "Influence of melt treatment and solidification parameters on the quality of 319.2 endchill aluminum castings," in *4th International Conference on Molten Aluminium Processing*, pp. 261–293, Orlando, FL, USA, November 1995.
- [28] J. Hernandez-Sandoval, A. M. Samuel, S. Valtierra, and F. H. Samuel, "Thermal analysis for detection of Zr-rich phases in Al-Si-Cu-Mg 354-type Alloys," *International Journal of Metalcasting*, vol. 11, no. 3, pp. 428–439, 2017.
- [29] J. Campbell and M. Tiryakioglu, "Review of effect of P and Sr on modification and porosity development in Al-Si alloys," *Materials Science and Technology*, vol. 26, no. 3, pp. 262–268, 2010.
- [30] R. Fuoco, E. R. Correa, and A. V. O. Correa, "Effect of modification treatment on microporosity formation in 356 Al alloy," *AFS Transactions*, vol. 103, pp. 379–387, 1995.
- [31] D. Argo and J. E. Gruzleski, "Porosity in modified aluminum alloy castings," *AFS Transactions*, vol. 96, pp. 65–74, 1988.
- [32] H. W. Kerr, J. Cisse, and G. F. Bolling, "On equilibrium and non-equilibrium peritectic transformations," *Acta Metallurgica*, vol. 22, pp. 677–686, 1974.
- [33] J. Murray, A. Peruzzi, and J. P. Abriata, "The Al-Zr (aluminum-zirconium) system," *Journal of Phase Equilibria*, vol. 13, no. 3, pp. 277–291, 1992.
- [34] U. Ikhlq, A. Hirose, R. Ahmad et al., "The role of Ar flow rates on synthesis of nanostructured zirconium nitride layer growth using plasma enhanced hot filament nitriding (PEHFN) technique," *The European Physical Journal Applied Physics*, vol. 69, no. 1, p. 10801, 2015.
- [35] K. E. Knipping, D. C. Dunand, and D. N. Seidman, "Precipitation evolution in Al-Zr and Al-Zr-Ti alloys during isothermal aging at 375–425°C," *Acta Materialia*, vol. 56, no. 1, pp. 114–127, 2008.
- [36] A. De Luca, S. Shua, and D. N. Seidman, "Effect of micro-additions of Mn and Mo on dual L12- and α -precipitation in a dilute Al-Zr-Sc-Er-Si alloy," *Materials Characterization*, vol. 169, pp. 114–127, 2020.
- [37] H. Basoalto and M. Anderson, "An extension of mean-field coarsening theory to include particle coalescence using nearest-neighbour functions," *Acta Materialia*, vol. 117, pp. 122–134, 2016.
- [38] J. Hernandez-Sandoval, G. H. Garza-Elizondo, A. M. Samuel, S. Valtierra, and F. H. Samuel, "The ambient and high temperature deformation behavior of Al-Si-Cu-Mg alloy with minor Ti, Zr, Ni additions," *Materials & Design*, vol. 58, pp. 89–101, 2014.
- [39] A. Rendtel, B. Moessner, and K. A. Schwetz, "Hardness and hardness determination in silicon carbide materials, book editor," *Advances in Ceramic Armor*, vol. 26, 2005.
- [40] A. Daoud and W. Reif, "Influence of Al₂O₃ particulate on the aging response of A356 Al-based composites," *Journal of Materials Processing Technology*, vol. 123, no. 2, pp. 313–318, 2002.
- [41] A. M. Samuel, H. Liu, and F. H. Samuel, "Effect of melt, solidification and heat-treatment processing parameters on the properties of Al-Si-Mg/SiC(p) composites," *Journal of Materials Science*, vol. 28, no. 24, pp. 6785–6798, 1993.
- [42] O. Prach, O. Trudonoshyn, P. Randelzhofer, C. Körner, and K. Durst, "Effect of Zr, Cr and Sc on the Al-Mg-Si-Mn high-pressure die casting alloys," *Materials Science and Engineering: A*, vol. 759, pp. 603–612, 2019.
- [43] G. H. Garza-Elizondo, A. M. Samuel, S. Valtierra, and F. H. Samuel, "Effect of Ni, Mn, Sc, and Zr addition on the tensile properties of 354-type Alloys at ambient temperature," *International Journal of Metalcasting*, vol. 11, no. 3, pp. 396–412, 2017.
- [44] R. L. Zhang, *Experiential Electronic Theory of Solid and Molecules Changchun*, Jilin Science and Technology Press, Changchun, China, 1993.
- [45] J. D. Robson and P. B. Prangnell, "Dispersoid precipitation and process modelling in zirconium containing commercial aluminium alloys," *Acta Materialia*, vol. 49, no. 4, pp. 599–613, 2001.